Identification of a Probable Pore-Forming Domain in the Multimeric Vacuolar Anion Channel AtALMT9[1][W][OPEN]

Jingbo Zhang[2], Ulrike Baetz[2], Undine Krügel, Enrico Martinoia, and Alexis De Angeli*

Institute of Plant Biology, University of Zürich, CH–8008 Zurich, Switzerland

Aluminum-**a**ctivated malate transporters (ALMTs) form an important family of anion channels involved in fundamental physiological processes in plants. Because of their importance, the role of ALMTs in plant physiology is studied extensively. In contrast, the structural basis of their functional properties is largely unknown. This lack of information limits the understanding of the functional and physiological differences between ALMTs and their impact on anion transport in plants. This study aimed at investigating the structural organization of the transmembrane domain of the Arabidopsis (*Arabidopsis thaliana*) vacuolar channel AtALMT9. For that purpose, we performed a large-scale mutagenesis analysis and found two residues that form a salt bridge between the first and second putative transmembrane α-helices (TMα1 and TMα2). Furthermore, using a combination of pharmacological and mutagenesis approaches, we identified citrate as an "open channel blocker" of AtALMT9 and used this tool to examine the inhibition sensitivity of different point mutants of highly conserved amino acid residues. By this means, we found a stretch within the cytosolic moiety of the TMα5 that is a probable pore-forming domain. Moreover, using a citrate-insensitive AtALMT9 mutant and biochemical approaches, we could demonstrate that AtALMT9 forms a multimeric complex that is supposedly composed of four subunits. In summary, our data provide, to our knowledge, the first evidence about the structural organization of an ion channel of the ALMT family. We suggest that AtALMT9 is a tetramer and that the TMα5 domains of the subunits contribute to form the pore of this anion channel.

The transport of ions across cellular membranes is mediated by specialized proteins that catalyze the transfer of charged molecules across hydrophobic lipid bilayers. Based on the thermodynamics, two major classes of transport systems can be distinguished: (1) passive transporters such as ion channels, which catalyze the flux of solutes down the electrochemical gradient, and (2) active transporters like pumps and antiporters, which transport molecules against their electrochemical gradient. Independent of the nature of the transport system, the flux of ions across membranes is crucial for a wide range of physiological functions in plants. Among others, ion transport is involved in intracellular pH regulation, metal tolerance, stomatal movement, cellular signaling, plant nutrition, and cell expansion (Roelfsema and Hedrich, 2005; Kim et al., 2010; Barbier-Brygoo et al., 2011). Despite the importance of anion transport in plant physiology, only in the last decade has the molecular identity of anion transport proteins started to be unveiled by identifying the chloride channel (CLC), slow anion channel (SLAC), and aluminum-activated malate transporter (ALMT) families. Their discovery has been a fundamental breakthrough in understanding the molecular mechanisms of anion homeostasis and its roles in various aspects of plant cell physiology (Ward et al., 2009; Barbier-Brygoo et al., 2011; Hedrich, 2012; Martinoia et al., 2012).

The CLC family consists of both anion channels and secondary active transporters, which are ubiquitously expressed in all living organisms. In Arabidopsis (*Arabidopsis thaliana*), the first identified and characterized member of the family was AtCLCa (Hechenberger et al., 1996; Geelen et al., 2000). AtCLCa is targeted to the tonoplast and acts as a $2NO_3^-/H^+$ antiporter (De Angeli et al., 2006). In planta, AtCLCa represents a major vacuolar nitrate transporter driving the accumulation of this anion into the vacuole. Subsequent studies revealed that all other Arabidopsis CLCs are likewise localized in intracellular membranes but feature different cellular functions (Barbier-Brygoo et al., 2011).

The SLAC protein family was identified in the last decade (Negi et al., 2008; Vahisalu et al., 2008). Despite its recent discovery, the characterization of this plant anion transporter family proceeded rapidly (Negi et al., 2008; Vahisalu et al., 2008; Geiger et al., 2009, 2010; Brandt et al., 2012). SLAC1, the first identified member of the family, is involved in slow-type anion currents across the plasma membrane of plant cells (Negi et al., 2008; Vahisalu et al., 2008). This ion channel is expressed in guard cells, where it mediates the efflux of anions into the apoplast, a process that is

[1] This work was supported by the Chinese Scholarship Council (to J.Z.), by a long-term EMBO fellowship (to A.D.A.), and by the Swiss National Foundation (to U.B., E.M., and A.D.A.).

[2] These authors contributed equally to the article.

* Address correspondence to deangeli.alexis@gmail.com.

The author responsible for distribution of materials integral to the findings presented in this article in accordance with the policy described in the Instructions for Authors (www.plantphysiol.org) is: Alexis De Angeli (deangeli.alexis@gmail.com).

[W] The online version of this article contains Web-only data.

[OPEN] Articles can be viewed online without a subscription.

www.plantphysiol.org/cgi/doi/10.1104/pp.113.219832

fundamental for stomata closure. SLAC1 regulates the stomatal aperture in response to different stimuli such as abscisic acid and high CO_2 and ozone concentrations (Negi et al., 2008; Vahisalu et al., 2008). In addition, the activity of SLAC1 is controlled by different kinases (Geiger et al., 2009, 2010) that are part of various signaling pathways. This multiple regulation of SLAC1 suggests that it plays a critical role in the integration of different environmental stimuli.

ALMTs are membrane proteins exclusive to plants. In Arabidopsis, this family consists of 14 members that can be grouped into three clades (Kovermann et al., 2007). The first member of the ALMT family, TaALMT1, was identified in wheat (*Triticum aestivum*) by Sasaki et al. (2004) when screening for genes associated with aluminum resistance. They provided evidence that TaALMT1 as well as AtALMT1, its homolog in Arabidopsis, are channels that catalyze the efflux of malate across the plasma membrane of root cells (Yamaguchi et al., 2005; Hoekenga et al., 2006). This exudation of organic acids into the soil facilitates the detoxification of environmental Al^{3+}. Besides contributing to Al^{3+} tolerance, ALMTs have been found to exhibit other important physiological functions. AtALMT12 has been proposed to mediate rapid anion currents across the plasma membrane of guard cells in order to induce stomata closure (Meyer et al., 2010). AtALMT9 and AtALMT6 have been shown to be channels localized in the tonoplast that mediate the export of malate into the vacuole (Kovermann et al., 2007; Meyer et al., 2011). AtALMT6 is predominantly expressed in guard cells, where its activity is regulated by cytosolic Ca^{2+} and vacuolar pH (Meyer et al., 2011). In contrast, AtALMT9 is widely expressed in several plant tissues, such as the mesophyll and guard cells. Recently, AtALMT9 was shown to play a crucial role in stomata movement, where it functions as a malate-activated chloride channel (De Angeli et al., 2013).

The knowledge about ion channel structures has expanded considerably in the last 20 years. Notably, various three-dimensional structures of such proteins have been solved (Choe, 2002; Jentsch, 2008; Traynelis et al., 2010). This has boosted the research into and the understanding of structure-function relations in transport systems. Among the anion channel families described above, the structure has been determined for CLCs (Dutzler et al., 2002) and SLACs (Chen et al., 2010). Additionally, large structure-function analyses have been conducted, providing detailed knowledge on the molecular basis underlying the ion channel functionality of these families. In contrast, little information was revealed about the structure of ALMTs by describing an important phosphorylation site (Ligaba et al., 2009; Furuichi et al., 2010) and by providing data on the topology (Motoda et al., 2007; Dreyer et al., 2012). However, the proposed models in these studies do not entirely coincide regarding the number of transmembrane-spanning domains, the cellular orientation of the N terminus, and the organization of the C-terminal domain. Therefore, the structural organization of ALMTs is still ambiguous.

In this study, we performed a large-scale mutagenesis analysis of the transmembrane domain (TMD) of Arabidopsis ALMTs using the vacuolar channel AtALMT9 as a model. The aim was to identify regions of the TMD that potentially exhibit functional relevance by forming the pore or the voltage sensor. For that purpose, we took advantage of citrate, which we identified as an open channel blocker of AtALMT9. The use of this blocker allowed elucidation of the structural details of ion channels, such as the quaternary organization and pore-forming domains, when no crystal structure was available (MacKinnon, 1991; Yellen et al., 1991; Ferrer-Montiel and Montal, 1996; Linsdell, 2005). By this means, it is possible to show, for instance, that potassium channels are tetramers and to identify their "selectivity filter" domain (MacKinnon and Yellen, 1990; MacKinnon, 1991). Thus, by using citrate, we pharmacologically investigated structure-function relations in AtALMT9. We identified a region adjacent to and within the fifth putative TMD that is supposedly involved in forming the permeation pathway of AtALMT9. Moreover, we demonstrated that AtALMT9 is a multimeric channel of probably four subunits in which the monomers participate in forming the pore.

RESULTS

Citrate Inhibits AtALMT9-Mediated Malate Currents

Blocking agents represent a common tool as reporter molecules to analyze functional and structural features of ion channels. In an attempt to disclose a blocker of the vacuolar channel AtALMT9, we were guided by a previous finding in which citrate was suggested to competitively inhibit malate uptake across the tonoplast (Rentsch and Martinoia, 1991). In order to test whether citrate is a blocker of AtALMT9, we isolated vacuoles from transiently transformed tobacco (*Nicotiana benthamiana*) protoplasts that overexpressed AtALMT9-GFP (OE AtALMT9). We used the patch-clamp technique to measure macroscopic currents mediated by AtALMT9 in the cytosolic-side-out excised patch configuration (Fig. 1). To avoid rectification due to ion concentration gradients between the two sides of the patched membrane, we performed experiments in symmetric ionic conditions (100 mM $malate_{vac}$/100 mM $malate_{cyt}$). Patches obtained from OE AtALMT9 tobacco vacuoles displayed inward-rectifying malate currents with time-dependent relaxations and a mean amplitude of -1.44 ± 0.51 nA at -120 mV, as reported in previous studies (Fig. 1A; Table I; Kovermann et al., 2007; for convention details regarding the applied voltage, see "Materials and Methods"). Even though citric acid is to 97% a tricarboxylate at pH 7.5 and exhibits similarities to the dicarboxylate malate (Fig. 1B), we could not detect a

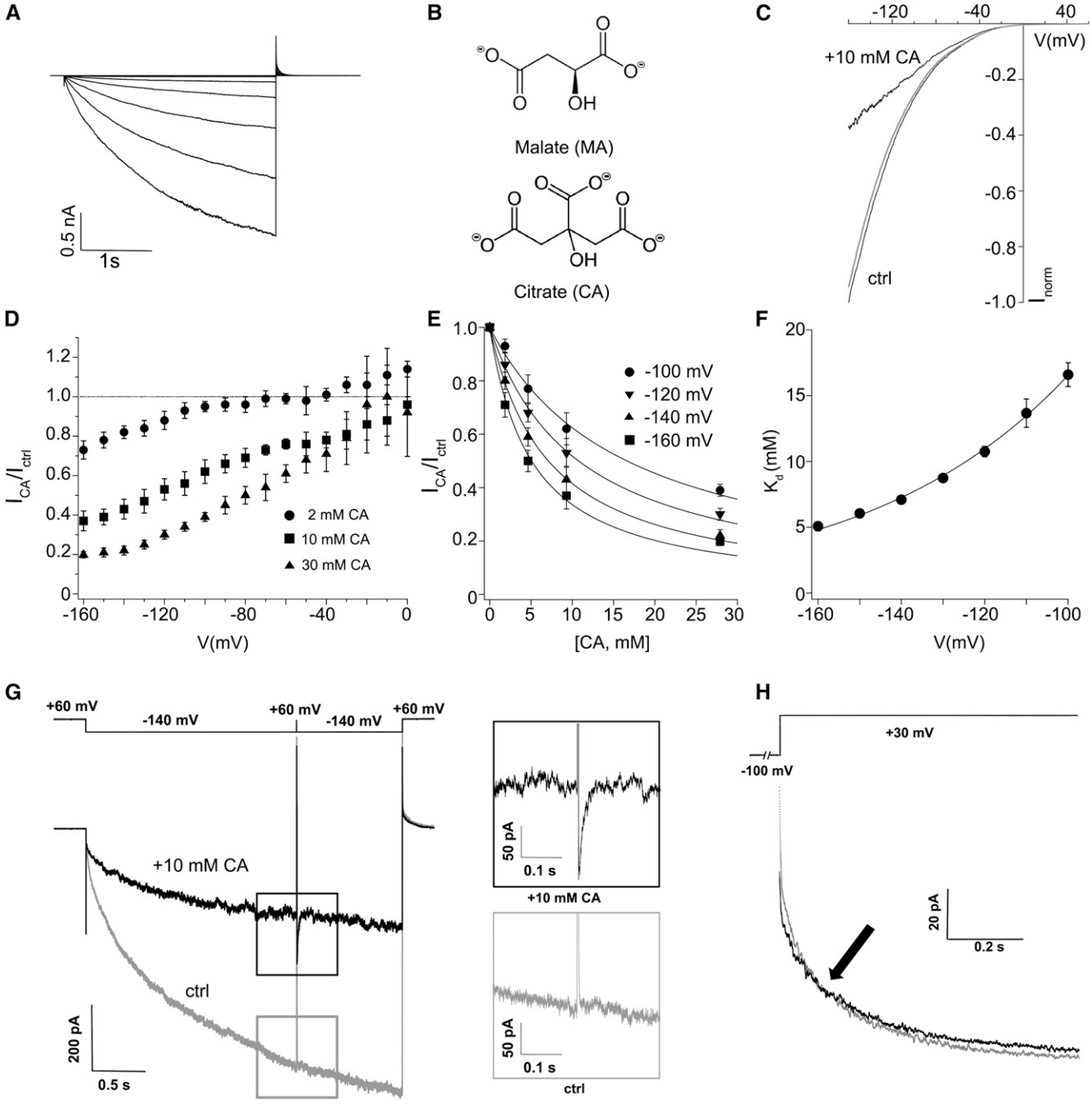

Figure 1. Citrate is a blocker of AtALMT9-mediated malate currents. A, Typical time-dependent currents from excised cytosolic-side-out patches obtained from AtALMT9-overexpressing tobacco vacuoles in symmetric malate conditions (100 mM $malate_{vac}$/100 mM $malate_{cyt}$). Currents were evoked in response to 3-s voltage pulses ranging from +60 mV to −120 mV in 20-mV steps, followed by a tail pulse at +60 mV, with a holding potential at +60 mV. B, Molecular structure of L-malate (MA) and citrate (CA) acids. C, Reversible inhibition of $AtALMT9_{WT}$ currents by 10 mM $citrate_{cyt}$. Normalized current-voltage curves were obtained with a voltage ramp (from +60 to −160 mV in 1.5 s) in cytosolic control solution (ctrl; 100 mM $malate_{cyt}$) and after adding 10 mM $citrate_{cyt}$ (100 mM $malate_{cyt}$ + 10 mM $citrate_{cyt}$). The gray line indicates the recovery in control cytosolic solution. D and E, Ratios between currents recorded in control and $citrate_{cyt}$-containing solutions (I_{CA}/I_{ctrl}) when using different $citrate_{cyt}$ concentrations (n = 4–5). E, Dose-response curves for $citrate_{cyt}$ at different potentials. Solid lines are fits obtained with Equation 1. F, Voltage dependency of the $K_d^{citrate}$. Solid lines correspond to data fitted with Equation 3. G, Representative current recording of a kick-out experiment on AtALMT9-meditated current. The currents were evoked using the voltage pulse protocol shown above the current traces. After the 3-ms pulse at +60 mV, a transient decrease of the current is observable in the presence of 10 mM $citrate_{cyt}$ (black trace inset). In contrast, in cytosolic control solution (gray trace inset), no transient decrease is

Table I. *Properties of wild-type and mutant AtALMT9 channels expressed in tobacco*

Data are presented as means ± SD.

chunK-Sample	I(nA) at −120 mV[a]	No. of Experiments	Conductive	$I_{citrate}/I_{ctrl}$ at −160 mV[b]	$K_d^{citrate}$ at −160 mV[c]	Rectification Rate[d]
					mM	
Untransformed	−0.06 ± 0.03	3	No	–	–	–
$AtALMT9_{WT}$	−1.44 ± 0.51****	11	Yes	0.37 ± 0.05	5.1 ± 0.3	0.19 ± 0.03
K87E	−1.52 ± 0.30**	4	Yes	0.59 ± 0.03****	16.2 ± 2.3	0.22 ± 0.02
K87R	−0.92 ± 0.06***	3	Yes	0.39 ± 0.04	–	–
K93E	−0.11 ± 0.04	5	No	–	–	–
K93A	−0.07 ± 0.03	4	No	–	–	–
K93N	−0.09 ± 0.04	3	No	–	–	–
K93R	−0.80 ± 0.42*	4	Yes	–	–	–
E130A	−0.07 ± 0.01	3	No	–	–	–
E130D	−1.28 ± 0.15****	5	Yes	–	–	–
E130K	−0.13 ± 0.07	4	No	–	–	–
K139E	−1.1 ± 0.15**	3	Yes	0.42 ± 0.04	–	0.16 ± 0.01
R143E	−0.10 ± 0.07	3	No	–	–	–
R143N	−0.09 ± 0.06	3	No	–	–	–
K187E	−0.09 ± 0.08	3	No	–	–	–
K187N	−0.07 ± 0.04	4	No	–	–	–
K193E	−1.46 ± 0.62**	7	Yes	0.99 ± 0.02****	–	0.50 ± 0.09***
K193A	−1.75 ± 0.25****	5	Yes	0.82 ± 0.02****	–	0.24 ± 0.03*
K193N	−0.63 ± 0.14*	3	Yes	0.83 ± 0.03****	–	0.29 ± 0.06*
K193R	−0.94 ± 0.43*	4	Yes	0.39 ± 0.04	–	0.16 ± 0.04
E196A	−0.87 ± 0.26***	6	Yes	0.39 ± 0.06	–	–
R200N	−1.43 ± 0.58**	5	Yes	0.86 ± 0.04****	–	0.18 ± 0.05
R200E	−0.12 ± 0.05	3	No	–	–	–
R200K	−0.62 ± 0.12*	3	Yes	0.38 ± 0.03	–	0.21 ± 0.02
R215E	−0.07 ± 0.03	3	No	–	–	–
R215N	−0.69 ± 0.27*	4	Yes	0.37 ± 0.04	–	0.14 ± 0.01**
R226E	−0.09 ± 0.06	3	No	–	–	–
R226N	−0.14 ± 0.08	4	No	–	–	–
K93E/E130K	−1.30 ± 0.27*	3	Yes	0.37 ± 0.02	–	–

[a]Current measured in 100 mM $malate_{cyt}$/100 mM $malate_{vac}$. Asterisks indicate statistically significant differences from untransformed tobacco (*$P < 0.05$, **$P < 0.01$, ***$P < 0.001$, ****$P < 0.0001$; two-tailed Student's *t* test). [b]Ratio between the current measured in 100 mM $malate_{cyt}$ + 10 mM $citrate_{cyt}$ and the current measured in 100 mM $malate_{cyt}$. Asterisks indicate statistically significant differences from $AtALMT9_{WT}$ (****$P < 0.0001$; two-tailed Student's *t* test). [c]$K_d^{citrate}$ determined with Equation 1. [d]Rectification rate measured as described in the text. Asterisks indicate statistically significant differences from $AtALMT9_{WT}$ (*$P < 0.05$, **$P < 0.01$, ***$P < 0.001$; two-tailed Student's *t* test).

significant permeation of citrate through AtALMT9 ($I_{citrate}/I_{malate}$ = 5% ± 5%; Supplemental Fig. S1A), as shown for BnALMT1 and BnALMT2 (Ligaba et al., 2006). However, when 10 mM citrate was applied at the cytosolic side (100 mM $malate_{vac}$/100 mM $malate_{cyt}$ + 10 mM $citrate_{cyt}$), AtALMT9 malate currents were reversibly inhibited to residual 37% ± 5% of the original current at −160 mV (Fig. 1C). The inhibition of the ion flux induced by $citrate_{cyt}$ was dose and voltage dependent (Fig. 1, D and E). Notably, the inhibitory effect of $citrate_{cyt}$ on AtALMT9-mediated currents occurred more pronouncedly at more negative membrane potentials (Fig. 1, C and D). However, the inhibition by $citrate_{cyt}$ did not change the voltage dependency of the relative open probability of the channel (Supplemental Fig. S1B). This implies that $citrate_{cyt}$ inhibition does not originate from a shift in channel gating toward more negative membrane potentials. When further analyzing the dose response of $citrate_{cyt}$ inhibition at different applied potentials, we found that the dissociation constant of $citrate_{cyt}$ ($K_d^{citrate}$; 5.1 ± 0.3 mM at −160 mV) was voltage dependent (Fig. 1, E and F). This finding indicates that the inhibiting anion citrate experiences the applied transmembrane electrical field. Consequently, we could estimate that citrate penetrates approximately 17% of the applied transmembrane electrical field (Woodhull, 1973). This, in turn, suggests that the interaction between citrate and the channel occurs within the membrane-spanning domain of AtALMT9 and possibly within the conduction pathway.

Figure 1. (*Continued.*)
observable. H, Crossing of the tail currents at +30 mV in control conditions (gray trace) and in the presence of 10 mM $citrate_{cyt}$ (black trace). AtALMT9 currents were elicited by an activating prepulse at −100 mV for 2 s followed by a tail pulse at +30 mV (1 s), as depicted above the current traces. The holding potential was set to +60 mV. Error bars represent SD.

To obtain direct evidence that citrate acts as an open channel blocker by interacting with the pore of AtALMT9, we investigated whether citrate binds to the activated channel. In a first step, we performed "kick-out experiments" (Becker et al., 1996; Fig. 1G). This approach is based on the reversible dissociation of citrate from its binding site when applying a short voltage pulse to the activated AtALMT9 channel at which $citrate_{cyt}$ was shown to no longer effectively block AtALMT9 (i.e. $V_m \geq 0$ mV; Fig. 1C). The "kick-out pulse" was transient and adjusted in order to not influence the voltage-dependent gating of the channel (Fig. 1G). Consequently, the proportion of channels in an open configuration was stable during and after the kick-out pulse. Therefore, effects on the current after the kick-out pulse did not originate from effects on the channel gating but from reversible pore blocking. During the kick-out experiments, we first activated the channels with a voltage pulse at −140 mV for 2 s. Subsequently, we stepped for 3 ms to a positive membrane potential (+60 mV) and then restored the membrane potential to −140 mV again (Fig. 1G). When this protocol was applied in the presence of the cytosolic control buffer (100 mM $malate_{cyt}$), the 3-ms pulse to +60 mV did not induce any significant channel closure, since the current levels before and immediately after the pulse were indistinguishable (Fig. 1G, gray trace inset). Differently, when applying the same protocol in the presence of 10 mM $citrate_{cyt}$, the 3-ms pulse at +60 mV was followed by a transient increase of the current that relaxed rapidly to the prepulse current amplitude (the time constant of the current relaxation is $\tau = 11.5 \pm 0.4$ ms at −140 mV; Fig. 1G, black trace inset). This fast relaxation after the kick-out pulse reflected the reversible binding kinetic of citrate to the channel. Thus, the results confirmed that citrate is capable of blocking AtALMT9 by binding to the open channel configuration. Concurrently, as expected for channels blocked in the open configuration, deactivating tail currents relaxed more slowly in the presence of $citrate_{cyt}$ than in its absence because of the dissociation of the blocking agent prior to closure of the channel. Hence, the application of an open channel blocker like citrate generates a typical crossover of the tail currents (Clay, 1995; Fig. 1H). Taken together, these data strongly indicate that citrate is an open channel blocker and that its inhibitory effect is likely due to a block of the conduction pathway of AtALMT9.

Effects of Positively and Negatively Charged Amino Acid Residues on Pore Conductivity

Despite the fact that ALMT proteins are known and have been studied for many years, few experimental data are available on the structure-function level (Motoda et al., 2007; Furuichi et al., 2010; Mumm et al., 2013). In particular, no study was conducted to investigate the TMD of ALMTs so far. Based on in silico analyses (http://aramemnon.botanik.uni-koeln.de), AtALMT9 is predicted to consist of a TMD at the N terminus and a soluble C-terminal domain encompassing roughly half of the protein. The TMD is predicted to be formed by six putative transmembrane α-helices, whereby the N terminus exhibits an intracellular orientation (TMα1–TMα6; Fig. 2A). However, other arrangements, such as an inverse inside-outside structure or more α-helices, were also proposed (Motoda et al., 2007; Dreyer et al., 2012). We performed a multiple alignment throughout all members of the ALMT family in Arabidopsis and identified several conserved or partially conserved amino acids within the TMD (Fig. 2B; Supplemental Fig. S2). We focused predominantly on positively charged residues, since they were often found to be relevant for functional elements of ion channels (pore and voltage sensor; Linsdell, 2005; Catterall, 2010). Interestingly, in line with the positive-inside rule (von Heijne and Gavel, 1988), the cytosolic-facing moiety of AtALMT9 exhibits a higher number of positively charged residues compared with the vacuolar moiety. While eight positively charged residues (three Arg and five Lys residues) are located at the cytosolic moiety, only three conserved positive residues face the vacuolar side (Fig. 2, A and B). To analyze the role of these residues in the TMD of AtALMT9, we substituted them by site-directed mutagenesis and monitored the effects of the mutation at a functional level (Fig. 2, D and E; Table I).

We transiently expressed the AtALMT9-GFP mutant channels in tobacco and first analyzed their intracellular localization by confocal laser scanning microscopy to verify whether the introduced point mutations resulted in a mistargeting of the protein. Interestingly, none of the mutations had an effect on the vacuolar targeting of the AtALMT9 channel (Fig. 2C; Supplemental Fig. S3). Subsequently, we analyzed the functionality of the mutated derivatives of AtALMT9 by performing patch-clamp analysis under the same experimental conditions as described above (Fig. 1A). The analysis revealed that the individual residues impacted differently on channel functionality. The removal of the positive charge of conserved Lys and Arg residues and the negative charge of the conserved Glu predicted to be inside the TMDαs (Lys-93, Glu-130, Arg-143, Lys-187, and Arg-226) resulted in a loss of conductivity (Fig. 2, D and E; Table I). On the contrary, substituting other conserved positively and negatively charged residues predicted to be in the loops between the TMDαs (Lys-87, Lys-139, Lys-193, and Glu-196) apparently did not affect the functionality of AtALMT9. In fact, patches from vacuoles transformed with these mutants presented time-dependent inward-rectifying currents with amplitudes that are reminiscent of those observed for $AtALMT9_{WT}$ (Figs. 1A and 2, D and E; Table I). Interestingly, the mutation of the two amino acids Arg-200 and Arg-215, the charge of which is not entirely conserved among the Arabidopsis ALMTs, affected the functionality of AtALMT9 dependent on the introduced residue. When

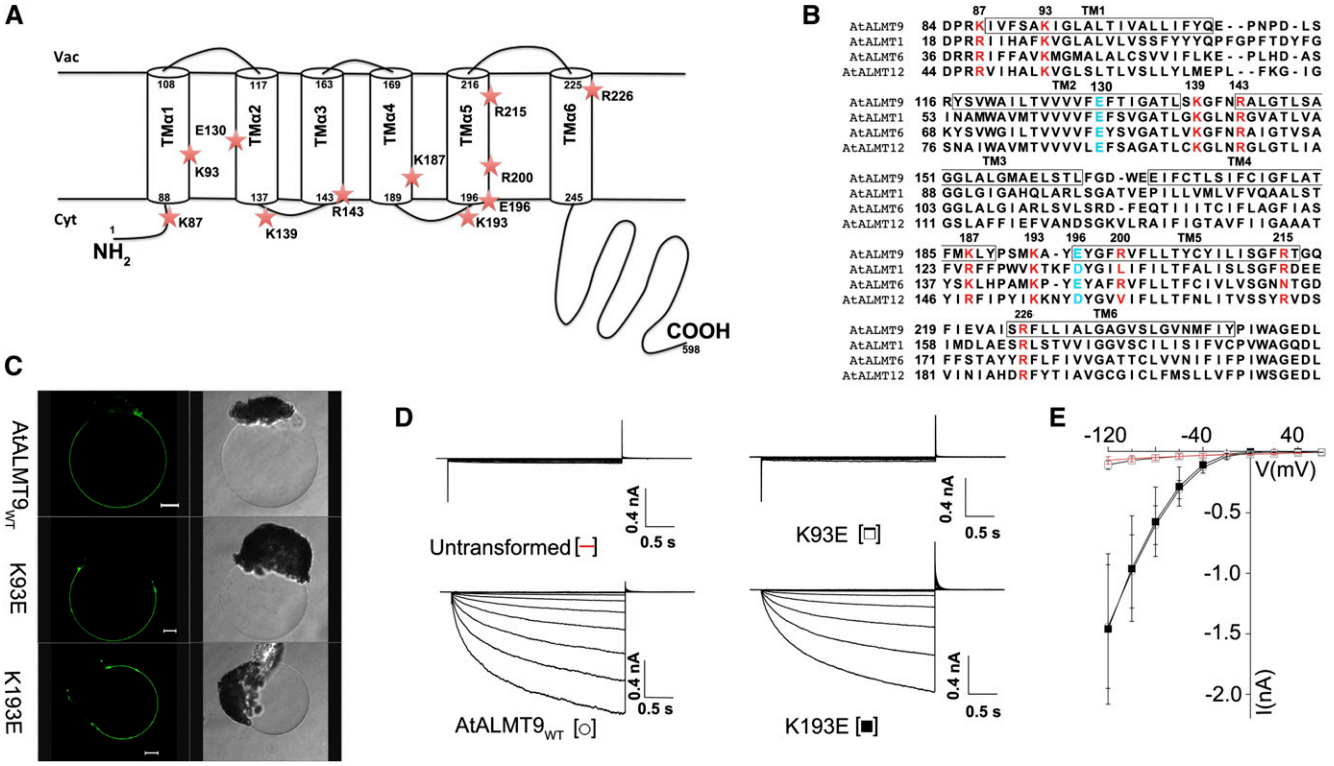

Figure 2. Impact of the mutation of conserved residues on AtALMT9 functionality. A, The TMD of AtALMT9 is predicted to be formed by six putative transmembrane α-helices (TMα1–TMα6) with the N terminus being located in the cytosol. The model illustrates the location of the amino acids targeted by site-directed mutagenesis (red stars). B, Multiple alignment of AtALMT9 with representative AtALMT proteins (AtALMT1, AtALMT6, and AtALMT12). The alignment was conducted with the Jalview software (Waterhouse et al., 2009). The black boxes indicate the predicted TMαs of AtALMT9. The conserved amino acids used for mutagenesis are displayed in red (positively charged residues) and in blue (negatively charged residues). C, Fluorescence and transmission images of vacuoles released from lysed tobacco mesophyll protoplasts transiently overexpressing AtALMT9$_{WT}$-GFP, AtALMT9$_{K93E}$-GFP, and AtALMT9$_{K193E}$-GFP imaged by confocal laser scanning microscopy. Bars = 10 μm. D, Representative current recordings of excised cytosolic-side-out patches of untransformed vacuoles as well as vacuoles overexpressing AtALMT9$_{WT}$, AtALMT9$_{K93E}$, and AtALMT9$_{K193E}$. Currents were evoked in response to 3-s voltage pulses ranging from +60 to −120 mV in 20-mV steps followed by a tail pulse at +60 mV. E, Mean current-voltage curves of untransformed vacuoles (red bars; n = 3), AtALMT9$_{WT}$ (white circles; n = 11), AtALMT9$_{K93E}$ (white squares; n = 5), and AtALMT9$_{K193E}$ (black squares; n = 7). In D and E, AtALMT9 currents were recorded in symmetric ionic conditions (100 mM malate$_{vac}$/100 mM malate$_{cyt}$). The holding potential was set to +60 mV. Error bars denote SD.

Arg-200 and Arg-215 were substituted with an Asn (AtALMT9$_{R200N}$ and AtALMT9$_{R215N}$), we observed time-dependent inward-rectifying currents comparable to AtALMT9$_{WT}$ (Table I; Supplemental Fig. S4, A and C). However, the introduction of a negatively charged residue like Glu (AtALMT9$_{R200E}$ and AtALMT9$_{R215E}$) led to nonfunctional channels (Table I; Supplemental Fig. S4, A and C). In summary, we observed three different effects on AtALMT9 channel functionality when mutating conserved charged residues. Four of the mutations we introduced induced a loss of conductivity, indicating that these residues were essential for the functionality of the channel. Furthermore, mutation of the cytosolic-facing residues did not influence channel functionality, whereas a third set of mutations resulted in a phenotype that was dependent on the introduced charge.

TMα1 and TMα2 Are Connected by a Salt Bridge

The analysis of the primary sequence alignment revealed two conserved charged residues arousing our interest. Lys-93 and Glu-130 are located within TMα1 and TMα2, respectively (Fig. 2, A and B). In the hydrophobic environment of membranes, unitary charges need to be stabilized by an interaction with a solvent and/or with an opposite charge (Perutz, 1978). When Glu-130 was replaced by an Ala or a Lys (AtALMT9$_{E130A}$ or AtALMT9$_{E130K}$), the channel was nonconductive, similar to AtALMT9$_{K93A}$ and AtALMT9$_{K93E}$ (Fig. 3; Table I). However, channels harboring conservative mutations in which the respective charge was kept (AtALMT9$_{K93R}$ and AtALMT9$_{E130D}$) displayed inward currents comparable to AtALMT9$_{WT}$ (Table I). Thus, we hypothesized that the two charged residues

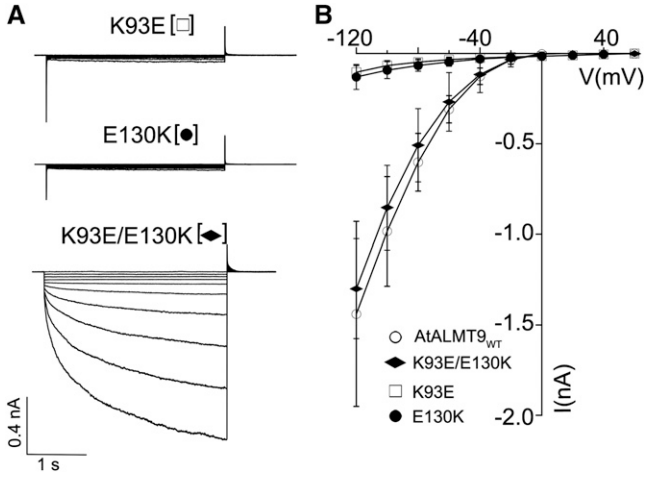

Figure 3. The conserved residues Lys-93 and Glu-130 form a salt bridge within the TMD of AtALMT9. A, Excised cytosolic-side-out current recordings from tobacco vacuoles overexpressing $AtALMT9_{K93E}$, $AtALMT9_{E130K}$, and the double mutant $AtALMT9_{K93E/E130K}$. Currents were evoked in response to 3-s voltage pulses ranging from +60 to −120 mV in 20-mV steps followed by a tail pulse at +60 mV. B, Mean current-voltage curves of malate currents mediated by $AtALMT9_{WT}$ (white circles; $n = 11$), $AtALMT9_{K93E/E130K}$ (black diamonds; $n = 3$), $AtALMT9_{K93E}$ (white squares; $n = 5$), and $AtALMT9_{E130K}$ (black circles; $n = 3$). Currents were recorded in symmetric conditions (100 mM $malate_{vac}$/100 mM $malate_{cyt}$). The holding potential was set to +60 mV. Error bars represent SD.

Lys-93 and Glu-130 could interact to form a salt bridge. To test this assumption, we generated a double mutant, $AtALMT9_{K93E/E130K}$, in which the charges of the amino acids Lys-93 and Glu-130 were exchanged. Astonishingly, the doubly mutated channel was functional and exhibited electrophysiological properties similar to $AtALMT9_{WT}$ (Fig. 3). $AtALMT9_{K93E/E130K}$ mediated currents with time-dependent relaxations and a mean amplitude of -1.30 ± 0.27 nA at −120 mV (Fig. 3B; Table I). Moreover, the double mutant was inhibited by citrate, as demonstrated for the $AtALMT9_{WT}$ channel (Table I; Supplemental Fig. S5). These results indicate that the positively charged Lys-93 and the negatively charged Glu-130 connect TMα1 and TMα2 by a salt bridge that is essential for the functionality of the channel.

Identification of Positively Charged Residues That Are Part of the Ion Conduction Pathway in AtALMT9

To investigate whether the mutated amino acids are possibly involved in forming the interaction site between citrate and the channel, we determined the sensitivity of the conductive AtALMT9 point mutants to citrate. The four charged residues Lys-87, Lys-139, Glu-196, and Arg-215 are located in the cytosolic loops next to TMα1, TMα2, and TMα5 and at the vacuolar-facing moiety of TMα5, respectively (Fig. 2, A and B). The channel derivatives $AtALMT9_{K87E}$, $AtALMT9_{K139E}$, $AtALMT9_{E196A}$, and $AtALMT9_{R215N}$ showed a moderate or no significant decrease in $citrate_{cyt}$ inhibition compared with $AtALMT9_{WT}$ [$(I_{citrate}/I_{ctrl})^{WT} = 0.37 \pm 0.05$, $(I_{citrate}/I_{ctrl})^{K87E} = 0.59 \pm 0.03$, $(I_{citrate}/I_{ctrl})^{K139E} = 0.42 \pm 0.04$, $(I_{citrate}/I_{ctrl})^{E196A} = 0.39 \pm 0.06$, and $(I_{citrate}/I_{ctrl})^{R215N} = 0.37 \pm 0.04$ at −160 mV; Fig. 4C; Table I]. In marked contrast, substitution of the residues Lys-193 and Arg-200, which reside at the cytosolic loop between TMα4 and TMα5 or within TMα5, respectively, reduced the $citrate_{cyt}$ blockade efficiency dramatically [$(I_{citrate}/I_{ctrl})^{K193N} = 0.83 \pm 0.03$ at −160 mV and $(I_{citrate}/I_{ctrl})^{R200N} = 0.86 \pm 0.04$ at −160 mV; Fig. 4; Table I]. Since the substitution R200E resulted in a nonfunctional channel, the effect of a negatively charged residue at this amino acid position could not be investigated. Nevertheless, the mutation K193E, which introduced a Glu, provided a conductive channel but caused a complete loss of $citrate_{cyt}$ inhibition ($I_{citrate}/I_{ctrl} = 0.99 \pm 0.02$ at −160 mV; Fig. 4, A and C). In addition, when performing kick-out experiments with the citrate-insensitive mutants $AtALMT9_{K193E}$ and $AtALMT9_{R200N}$, the kick-out pulse was not followed by fast-relaxing current transients (Supplemental Figs. S1D and S4B). Since the transient current relaxation is due to the rapid dissociation and subsequent binding of $citrate_{cyt}$ to the open channel configuration of $AtALMT9_{WT}$, its absence provided evidence that $citrate_{cyt}$ was not able to interact with the $AtALMT9_{K193E}$ and $AtALMT9_{R200N}$ mutant channels and did not enter the TMD in these mutants. In contrast, the citrate-sensitive channel $AtALMT9_{R215N}$, which possesses a substitution at the vacuolar-facing part of the membrane, exhibited a transient current relaxation comparable to the wild-type channel after applying a kick-out pulse (Supplemental Fig. S4D).

Taken together, these results indicate that the positively charged residues Lys-193 and Arg-200, which are located adjacent to or within TMα5, are involved in mediating the interaction of citrate with AtALMT9. Considering the fact that citrate acts as an open channel blocker, the data suggest that Lys-193 and Arg-200 are part of the ion conduction pathway of AtALMT9. To further confirm the pore-forming feature of the two residues and TMα5, we explored the functional properties of the conductive AtALMT9 mutants by analyzing the "open channel rectification." This parameter directly reflects the properties of the conduction pathway itself, excluding rectification effects based on voltage-dependent gating. To quantify the open channel rectification of $AtALMT9_{WT}$ and its derivatives, we made used of the rectification rate coefficient (Linsdell, 2005). This coefficient is defined as the ratio between the conductance measured at the end of the activation pulse at −120 mV and the conductance measured at the beginning of the tail pulse at +60 mV (for details, see "Materials and Methods"). The rectification ratio of $AtALMT9_{WT}$ was 0.19 ± 0.03, indicating that the conduction pathway of this channel had intrinsic inward rectification properties. Strikingly, we observed that the citrate-insensitive channel

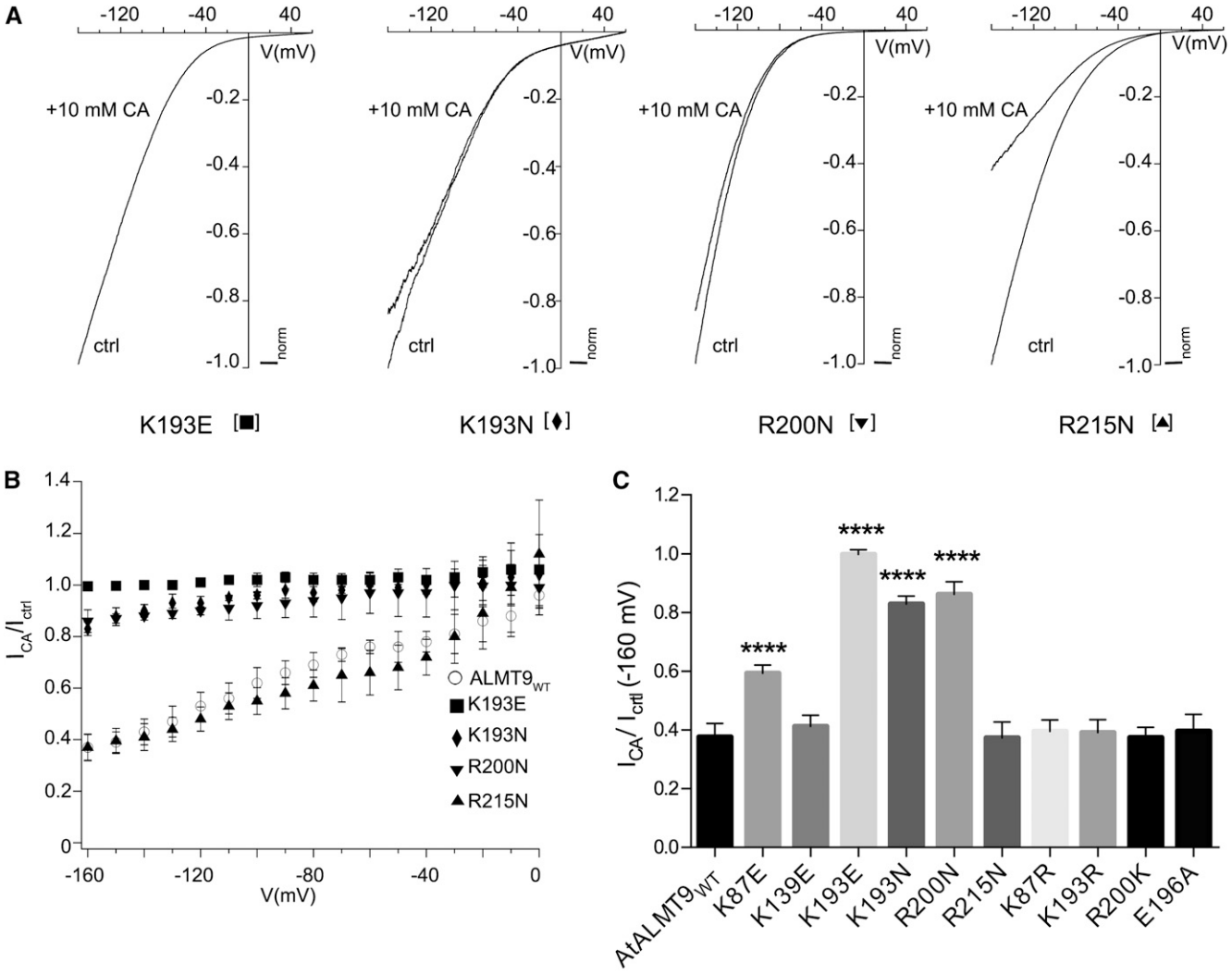

Figure 4. Variable effects of mutations of conserved AtALMT9 residues on citrate blockade. A, Normalized current-voltage curves of the mutants $AtALMT9_{K193E}$, $AtALMT9_{K193N}$, $AtALMT9_{R200N}$, and $AtALMT9_{R215N}$ in control conditions (ctrl) and in the presence of 10 mM $citrate_{cyt}$ (CA) obtained with a voltage ramp (from +60 mV to −160 mV in 1.5 s). B, Ratio between the control currents and the residual currents after inhibition with 10 mM $citrate_{cyt}$ (I_{CA}/I_{ctrl}). Depicted are $AtALMT9_{K193E}$ (squares; $n = 4$), $AtALMT9_{K193N}$ (diamonds; $n = 4$), $AtALMT9_{R200N}$ (inverted triangles; $n = 4$), $AtALMT9_{R215N}$ (triangles; $n = 3$), and $AtALMT9_{WT}$ (circles; $n = 4$). C, Ratios of the currents of different AtALMT9 mutants before and after the application of 10 mM $citrate_{cyt}$ (I_{CA}/I_{ctrl}; $n = 3$–5) at −160 mV. Currents were measured in symmetric conditions (100 mM $malate_{vac}$/100 mM $malate_{cyt}$). Asterisks indicate statistically significant differences from $AtALMT9_{WT}$ (****$P < 0.0001$; two-tailed Student's t test). Error bars denote SD.

$AtALMT9_{K193E}$, which was mutated in an amino acid residue of the pore region, and $AtALMT9_{R215N}$, which harbors a mutation within TMα5, exhibited an altered rectification ratio compared with $AtALMT9_{WT}$ (Table I). $AtALMT9_{K193E}$ showed a markedly increased rectification ratio of 0.50 ± 0.09, whereas $AtALMT9_{R215N}$ exhibited a lower rectification ratio (0.14 ± 0.01). The different rectification rates of $AtALMT9_{K193E}$ and $AtALMT9_{R215N}$ indicate that the mutated residues are involved in conferring rectification characteristics to the pore of AtALMT9. Hence, it is likely that Lys-193 and Arg-215 are involved in forming the conduction pathway. In summary, we could observe alterations in citrate block sensitivity and open channel rectification when analyzing the properties of the conductive mutant channels. We identified three positively charged residues preceding TMα5 or within TMα5 (Lys-193, Arg-200, and Arg-215) that fundamentally contribute to the functionality of the conduction pathway of AtALMT9.

AtALMT9 Is a Multimeric Anion Channel Composed of Four Subunits

The discovery of the mutant channel $AtALMT9_{K193E}$, which is characterized by complete insensitivity to

citrate inhibition, provides the opportunity to investigate whether AtALMT9 is a monomeric or a multimeric channel (MacKinnon, 1991; Kosari et al., 1998). If AtALMT9 is a monomer, a co-overexpression of $AtALMT9_{WT}$ and $AtALMT9_{K193E}$ would not influence the $K_d^{citrate}$. In contrast, in case AtALMT9 functions as a multimeric complex, the heteromultimeric hybrids of $AtALMT9_{WT}$ and $AtALMT9_{K193E}$ would exhibit an altered sensitivity to $citrate_{cyt}$. Therefore, the presence of heteromultimers would result in a shift in $K_d^{citrate}$. We performed experiments in which we coinfiltrated tobacco leaves with a mixture of two *Agrobacterium tumefaciens* strains carrying plasmids with the sequence of either $AtALMT9_{WT}$ or $AtALMT9_{K193E}$ in different ratios (1:1 and 1:4). First, we verified the transcription levels of $AtALMT9_{WT}$ and $AtALMT9_{K193E}$ after coinfiltration. When infiltrating leaves with a 1:1 ratio of the two *A. tumefaciens* strains, we observed that 50.1% ± 9.2% of the *AtALMT9* transcripts were of wild-type origin and 49.9% ± 9.2% were the mutant sequence. Similarly, when coinfiltrating tobacco leaves with the two *A. tumefaciens* strains in a ratio of 1:4, we found that 15% ± 13% of the *AtALMT9* transcripts were the wild-type sequence and 85% ± 13% showed the sequence of $AtALMT9_{K193E}$ (Fig. 5A). Thus, using these *A. tumefaciens* mixtures, we were able to coexpress both AtALMT9 variants in tobacco in a ratio corresponding to that of the infiltration mix. Subsequently, we tested the citrate block sensitivity of vacuoles co-overexpressing $AtALMT9_{WT}$ and $AtALMT9_{K193E}$ in 1:1 and 1:4 ratios. As observed in OE $AtALMT9_{WT}$ patches, the coexpression displayed

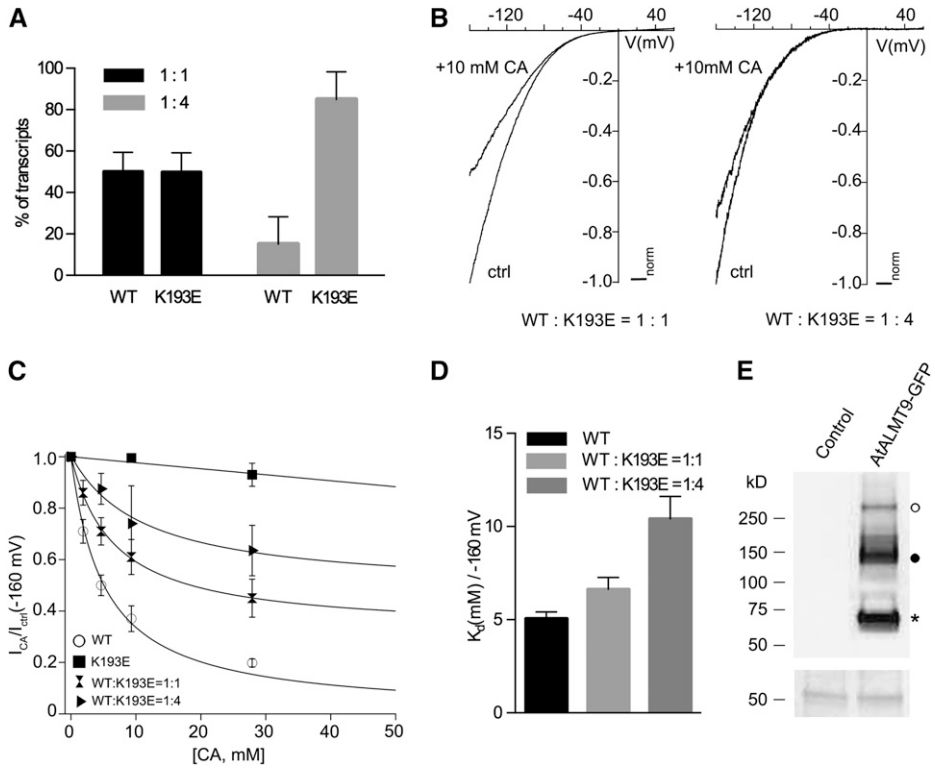

Figure 5. AtALMT9 forms homomultimeric complexes. A, Relative occurrence of $AtALMT9_{WT}$ and $AtALMT9_{K193E}$ transcripts in leaves of tobacco coinfiltrated with a 1:1 and a 1:4 mixture of *A. tumefaciens* strains each carrying plasmids with the sequence of one of the channel variants. Error bars represent SD of four biologically independent replicates (20 transcripts were analyzed for each replicate). B, Representative normalized current-voltage curves obtained with a voltage ramp (from +60 to −160 mV in 1.5 s; the holding potential was +60 mV) measured in excised cytosolic-side-out patches from vacuoles coexpressing $AtALMT9_{WT}$ and $AtALMT9_{K193E}$ at different ratios (left, $AtALMT9_{WT}$:$AtALMT9_{K193E}$ = 1:1; right, $AtALMT9_{WT}$:$AtALMT9_{K193E}$ = 1:4). Currents were recorded in control conditions (ctrl) and in the presence of 10 mM $citrate_{cyt}$ (CA). C, Dose-response curves for $citrate_{cyt}$ from vacuoles overexpressing $AtALMT9_{WT}$ (circles), $AtALMT9_{K193E}$ (squares), $AtALMT9_{WT}$:$AtALMT9_{K193E}$ = 1:4 (triangles), and $AtALMT9_{WT}$:$AtALMT9_{K193E}$ = 1:1 (hourglass; n = 4–7). The data of $AtALMT9_{WT}$ were fitted with Equation 1. Data of the 1:1 and 1:4 ratios were fitted with Equation 2. Error bars denote SD. D, Values of the $K_d^{citrate}$ at V_m = −160 mV derived from C. Currents were recorded in symmetric conditions (100 mM $malate_{vac}$/100 mM $malate_{cyt}$). Error bars display SD. E, Immunoblot analysis of microsomal proteins extracted from untransformed (control) and $AtALMT9_{WT}$-overexpressing (AtALMT9-GFP) leaves of tobacco using an anti-GFP antibody. In the top panel, the lane of protein extracts from AtALMT9-overexpressing leaves displays three bands corresponding to monomeric (star; approximately 70 kD), dimeric (black circle; approximately 140 kD), and tetrameric (white circle; approximately 280 kD) forms of the AtALMT9 protein complex. The bottom panel shows the corresponding Ponceau S staining. WT, Wild type.

malate currents that were blocked by $citrate_{cyt}$ (Fig. 5B). Notwithstanding, the currents in vacuolar patches co-overexpressing both AtALMT9 variants were less sensitive to $citrate_{cyt}$ than currents recorded in vacuoles only expressing $AtALMT9_{WT}$ and showed a shift in $K_d^{citrate}$ (Fig. 5C). The $K_d^{citrate}$ was 6.6 ± 0.6 mM and 10.4 ± 1.2 mM for the 1:1 and 1:4 ratios, respectively, thus representing 1.3- and 2.1-fold increases of $K_d^{citrate}$ compared with $AtALMT9_{WT}$ (Fig. 5D). This increase of $K_d^{citrate}$ in vacuoles simultaneously expressing $AtALMT9_{WT}$ and $AtALMT9_{K193E}$ is in agreement with a model in which both variants assemble to a heteromultimeric channel and citrate interacts with multiple subunits. To further confirm this finding, we performed denaturing PAGE on microsomal proteins extracted from transiently transformed tobacco leaves that overexpressed AtALMT9-GFP (Fig. 5E). Using a GFP-specific antibody, we detected AtALMT9-GFP predominantly as an approximately 70-kD monomer. This band was smaller than predicted based solely on its formula molecular mass (93.5 kD) but was consistent with an apparent reduction in protein size observed under nonreducing conditions (Wittig and Schägger, 2008). We identified two higher order complexes in the absence of reducing agents and without heating up the samples (Fig. 5E). These complexes corresponded in size to an AtALMT9-GFP dimer (approximately 140 kD) and a tetramer (approximately 280 kD; Fig. 5E). Thus, these results provide evidence that AtALMT9-GFP functions as a multimer in which supposedly four subunits form the channel.

DISCUSSION

The usage of blockers and the analysis of their effects on different site-specific mutants have allowed the development of structural models of ion channels when the crystal structures were not solved (MacKinnon, 1991; Yellen et al., 1991; Linsdell, 2005). Due to the absence of detailed data about the structure of ALMTs, the only available information comes from in silico predictions and a few structure-function studies (Motoda et al., 2007; Ligaba et al., 2009; Furuichi et al., 2010; Mumm et al., 2013). Hence, the exact topology of ALMT proteins is not yet unambiguously determined (Motoda et al., 2007; Dreyer et al., 2012). Nonetheless, on the basis of software predictions and the existing data, Arabidopsis ALMT channels are likely to be formed by an N-terminal TMD constituted of six membrane-spanning helices with the N-terminal and the C-terminal domains featuring an intracellular orientation (Fig. 2A; Kovermann et al., 2007; http://aramemnon.botanik.uni-koeln.de). Using in silico analysis, Piñeros et al. (2008) suggested that the TMD is involved in forming the permeation pathway. Nevertheless, the few structure-function studies focused on the C-terminal domain of ALMT proteins (Ligaba et al., 2009; Furuichi et al., 2010; Mumm et al., 2013). Because of the complete lack of experimental data on the N-terminal TMD of ALMTs, we performed a site-directed mutagenesis screen of this region using AtALMT9.

We could identify the three residues Lys-193, Arg-200, and Arg-215 as being important for channel functionality and possibly as being part of the anion conduction pathway. The mutation of Lys-193 and Arg-200, which are localized at the cytosolic face of AtALMT9, strongly impacted on both channel functionality and citrate blockade. The channel variants $AtALMT9_{K193N}$ and $AtALMT9_{K193E}$ display a strong and progressive effect on citrate inhibition sensitivity, resulting in a complete abolition of the open channel blockade in $AtALMT9_{K193E}$. Moreover, $AtALMT9_{K193E}$ features an impaired open channel rectification compared with $AtALMT9_{WT}$. Regarding position Arg-200, the substitution into a Glu results in a nonconductive channel ($AtALMT9_{R200E}$), while the channel variant $AtALMT9_{R200N}$ is functional but has strongly reduced citrate block sensitivity. Differently, mutation of the

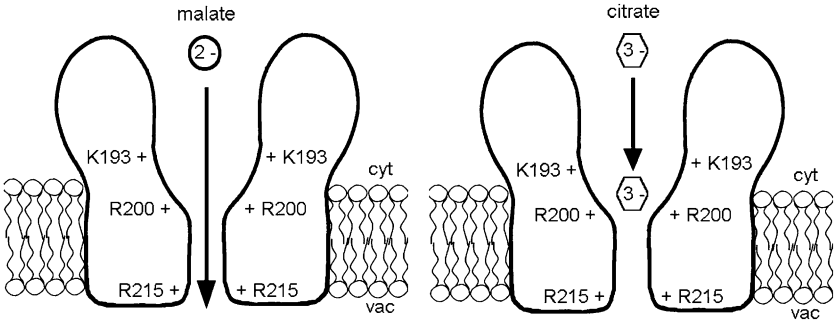

Figure 6. Model illustrating the block of AtALMT9 by cytosolic citrate. Cytosolic citrate inhibits AtALMT9 by acting as an open channel blocker. This indicates that citrate enters the permeation pathway to block AtALMT9 currents. To exert its blocking action, the trivalent anion citrate interacts electrostatically with the two positively charged residues Lys-193 and Arg-200. Lys-193 and Arg-200 are located at the cytosolic side of the channel and are likely to participate in forming the pore entrance. The vacuolar-facing Arg-215 is involved in the anion permeation process through AtALMT9 and, like Lys-193 and Arg-200, is part of the same putative transmembrane helix (TMα5).

residue Arg-215, as expected by its predicted vacuolar-side localization, does not modify citrate inhibition. However, $AtALMT9_{R215N}$ is impaired in its rectification ratio, suggesting that the mutated residue is involved in the permeation process. Again, an exchange of the electrical charge of the residue (R215E) results in a nonconductive channel. Interestingly, the charge conservative mutant channels of these three positions ($AtALMT9_{K193R}$, $AtALMT9_{R200K}$, and $AtALMT9_{R215K}$) maintained the channel properties indistinguishable from $AtALMT9_{WT}$ (Fig. 4C). Therefore, the interaction of citrate with AtALMT9 is mainly electrostatic, and Lys-193 and Arg-200 are key residues in forming the citrate-binding site. When inhibiting AtALMT9 currents, citrate enters the TMD and penetrates 17% of the applied electrical field. Thus, combining this information with the predicted location of Lys-193 and Arg-200, it is likely that the binding site for citrate is placed at the cytosolic entrance of the conduction pathway of AtALMT9 (Fig. 6).

In addition, the results provided information about the topology of the AtALMT9 TMD. Our experimental data point toward an opposite orientation of ALMT proteins compared with the models proposed by Motoda et al. (2007) and Dreyer et al. (2012). Indeed, the fact that the mutation of the cytosolic-facing residues Lys-87, Lys-193, and Arg-200 impairs citrate block (Fig. 4; Supplemental Fig. S4) while the mutation of the vacuolar-facing Arg-215 does not is in agreement with the computer-based prediction of the topology of AtALMT9, with an intracellular localization of the N terminus and an orientation of the protein as depicted in Figure 2. Moreover, this study demonstrates that three residues (Lys-193, Arg-200, and Arg-215) that are important in the anion permeation process reside within TMα5 or in the short loop preceding it. TMα5 is predicted to span the entire membrane, whereby Lys-193 and Arg-200 are located on the opposite side of TMα5 than Arg-215 (Fig. 2). Hence, it is tempting to speculate that TMα5 lines the whole permeation pathway of AtALMT9, similar to what has been previously observed in other ion channels (Hilf and Dutzler, 2009; Hibbs and Gouaux, 2011).

Several introduced mutations of residues in the TMD result in major defects on AtALMT9 conductivity regardless of the chemical properties of the substitution (Table I). This nonfunctionality prevents further investigations but suggests an essential structural role of these residues. Nonetheless, we have identified the distinct structural role of the residue Lys-93. Lys-93 is located within TMα1 and is strictly conserved among different ALMTs (Supplemental Fig. S2). We have demonstrated that Lys-93 forms a salt bridge with another strictly conserved residue in TMα2, Glu-130. This proves that TMα1 and TMα2 are connected by a salt bridge that is crucial for channel functionality. Similar observations of a restored wild-type channel function when exchanging the residues of a salt bridge have been made in the cystic fibrosis transmembrane conductance regulators (Cotten and Welsh, 1999; Cui et al., 2013).

The concomitant finding of the pore blocker citrate and the mutant channel $AtALMT9_{K193E}$ that features abolished block sensitivity allowed investigation of the oligomeric state of AtALMT9 (MacKinnon, 1991). This is an intriguing opportunity, since, to our knowledge, it is not known whether ALMTs present a monomeric or multimeric architecture. To distinguish between these two possibilities, we coexpressed $AtALMT9_{WT}$ and $AtALMT9_{K193E}$ and found that the sensitivity to citrate was decreased and the $K_d^{citrate}$ was shifted. These results are consistent with a model in which AtALMT9 channels form a multimeric complex and citrate interacts with multiples of those subunits. Moreover, since citrate is an open channel blocker interacting with the pore-forming region, our data suggest that several AtALMT9 polypeptides participate in forming the anion conduction pathway. This type of multimeric organization is shared with several other families of ion channels like potassium channels (MacKinnon, 1991), Glu receptors (Rosenmund et al., 1998; Robert et al., 2001), and acid-sensing channels (Kosari et al., 1998, 2006; Snyder et al., 1998). However, due to the low affinity of citrate, it is not possible to apply saturating blocker concentrations that would have allowed determination of the exact stoichiometry of AtALMT9 complexes. Therefore, we used a biochemical approach to provide evidence that AtALMT9 features a multimeric organization. Our data suggest that AtALMT9 forms presumably tetrameric complexes, similar to what has been found for potassium channels (Daram et al., 1997; Doyle et al., 1998). These results are in line with recent findings on AtALMT9, where the induction of chloride conductance by malate was shown to exhibit a Hill coefficient of 2.5, indicating that more than two subunits are required to form a functional channel (De Angeli et al., 2013).

One question that arises from this ensemble of results is whether the structural characteristics we described for AtALMT9 are extendible to other members of the ALMT family. We predominantly investigated residues that are conserved among the family at least in their electrical charge. Moreover, based on secondary structure prediction, the N-terminal TMD has a remarkably conserved topology. Thus, it is probable that the results concerning the structure found for one ALMT are also valid for other members.

In conclusion, our work provides new molecular, biochemical, and biophysical details about the TMD of a member of the ALMT family. We identified a probable pore-forming region of ALMT anion channels and revealed that AtALMT9, and presumably also other ALMTs, are multimeric complexes formed by four subunits in which multiple subunits participate in the formation of the conduction pathway.

MATERIALS AND METHODS

Site-Directed Mutagenesis

Arabidopsis (*Arabidopsis thaliana*) AtALMT9 complementary DNA was cloned into the expression vector pART27 as described previously (Kovermann

et al., 2007). The site-directed mutants were generated following the manufacturer's instructions of the Quikchange Site-Directed Mutagenesis Kit (Agilent Technologies) with slight modifications. All point mutations were verified by sequencing.

Overexpression of AtALMT9-GFP in Tobacco

Agrobacterium tumefaciens (GV3101) was transformed with plasmids containing the sequences of the $AtALMT9_{WT}$ channel and its point-mutated derivatives by electroporation. The *A. tumefaciens*-mediated infiltration of 4-week-old tobacco (*Nicotiana benthamiana*) leaves was performed as described previously with slight modifications (Yang et al., 2001). After transient transformation, tobacco plants were grown in the greenhouse (16 h of light/8 h of dark, 25°C/23°C, 100–200 μmol photons m^{-2} s^{-1}, 60% relative humidity) for another 2 to 3 d and then used to isolate protoplasts for confocal laser scanning microscopy and patch-clamp experiments.

Verification of $AtALMT9_{WT}$ and $AtALMT9_{K193E}$ Coexpression in Tobacco

A. tumefaciens strains harboring plasmids with either the sequence of $AtALMT9_{WT}$ or $AtALMT9_{K193E}$ were coinfiltrated into tobacco in a bacteria ratio of 1:1 and 1:4 after defining the optical density at 600 nm. Whole-leaf RNA was extracted 2 to 3 d after transient transformation, and complementary DNA was subsequently synthesized. We amplified *AtALMT9* via PCR using a 20-μL reaction volume and the Phusion High-Fidelity DNA Polymerase (Thermo Scientific). PCR conditions were set as follows: 98°C for 2 min in the first cycle; subsequently, 30 amplification cycles consisting of 10 s at 98°C, 20 s at 58°C, and 1.20 min at 72°C; the final extension was 5 min at 72°C. Subsequently, we cloned the PCR product into the pJet1.2/blunt cloning vector (CloneJet PCR Cloning Kit; Thermo Scientific) and determined the amount of $AtALMT9_{WT}$ and $AtALMT9_{K193E}$ transcripts by sequencing.

Microscopy

Intracellular localization of AtALMT9-GFP mutants was determined by performing a lysis to release vacuoles of tobacco protoplasts overexpressing the appropriate mutant channel construct. Microscopy was conducted using a Leica DMIRE2 www.leica-microsystems.com laser scanning microscope that was equipped with a 63× glycerol objective. GFP fluorescence signal was imaged at an excitation wavelength of 488 nm, and the emission was detected between 500 and 530 nm. The appropriate Leica confocal software has been used for image acquisition. The images in Supplemental Figure S3 were obtained with an epifluorescence microscope (Nikon Eclipse TS100) and acquired with a digital camera (Nikon DS-Fi1).

Electrophysiology

Mesophyll protoplasts from AtALMT9-GFP-overexpressing tobacco leaves were isolated by enzymatic digestion. The enzyme solution contained 0.3% (w/v) cellulase R-10, 0.03% (w/v) pectolyase Y-23, 1 mM $CaCl_2$, 500 mM sorbitol, and 10 mM MES, pH 5.3, 550 mosmol. Protoplasts were washed twice and resuspended in the same solution without enzymes. Vacuoles were released from mesophyll protoplast by the addition of 5 mM EDTA and a slight osmotic shock (500 mosmol; see medium below). Transformed vacuoles exhibiting an AtALMT9-GFP signal were selected using an epifluorescence microscope. Membrane currents from patches of the tonoplast were recorded using the excised cytosolic-side-out patch-clamp technique as described elsewhere (De Angeli et al., 2013). Briefly, currents were recorded with an EPC10 patch-clamp amplifier (HEKA Electronics) using Patchmaster software (HEKA Electronics). Data were analyzed with FitMaster software (HEKA Electronics). In experiments on macroscopic current recordings, the pipette resistance was 4 to 5 MΩ. Only patches presenting a seal resistance higher than 2 GΩ were used to perform experiments. Macroscopic current recordings were filtered at 300 Hz.

The pipette solution contained 112 mM malic acid and 5 mM HCl and was adjusted with BisTrisPropane (BTP) to pH 6. The osmolarity was adjusted with sorbitol to 550 mosmol. The bath solution contained (1) 100 mM malic acid, 3 mM $MgCl_2$, and 0.1 mM $CaCl_2$, adjusted to pH 7.5 with BTP; (2) 100 mM malic acid, citric acid (2, 5, 10, or 30 mM), 3 mM $MgCl_2$, and 0.1 mM $CaCl_2$, adjusted to pH 7.5 with BTP; and (3) 100 mM citric acid, 3 mM $MgCl_2$, and 0.1 mM $CaCl_2$, adjusted to pH 7.5 with BTP. The osmolarity was adjusted to 500 mosmol using sorbitol. All chemicals were purchased from Sigma-Aldrich. Liquid junction potentials were measured and corrected when higher than ±2 mV (Neher, 1992). Current-voltage characteristics were obtained by subtracting the current at time zero from the quasistationary currents (averaging the last 50 ms of the current trace) elicited by main voltage pulses. In all patch-clamp experiments, the applied membrane potential (V_m) is presented according to the convention for intracellular organelles of Bertl et al. (1992), namely $V_m = V_{cyt} - V_{vac}$, where V_{cyt} and V_{vac} are the cytosolic and vacuolar potentials, respectively.

The dose response for the $citrate_{cyt}$ inhibition of $AtALMT9_{WT}$ currents (Figs. 1 and 5; Supplemental Fig. S4) was fitted and analyzed with the Langmuir isotherm in the following form:

$$\frac{I}{I_0} = 1 - \frac{1}{1 + \frac{K_d^{CA}}{[CA]_{cyt}}} \quad (1)$$

where I is the AtALMT9 current amplitude in the presence of $citrate_{cyt}$, I_0 is the AtALMT9 current under control solution, $[CA]_{cyt}$ is the cytosolic citrate concentration, and K_d^{CA} is the dissociation constant of citrate.

The dose response for the $citrate_{cyt}$ inhibition of the co-overexpression of $AtALMT9_{WT}$ and $AtALMT9_{K193E}$ in 1:1 and 1:4 ratios (Fig. 5) was fitted with the Langmuir isotherm in the following form:

$$\frac{I}{I_0} = 1 - \frac{I_{inh}}{1 + \frac{K_d^{CA}}{[CA]_{cyt}}} \quad (2)$$

where I is the current amplitude in the presence of $citrate_{cyt}$, I_0 is the current amplitude under control solution, $[CA]_{cyt}$ is the cytosolic citrate concentration, K_d^{CA} is the dissociation constant of citrate, and I_{inh} is the maximum fraction of current inhibited by $citrate_{cyt}$.

To estimate the fraction of the electrical field that citrate traverses to reach its binding site, the voltage-dependent dissociation constant relationship was fitted with the equation described by Woodhull (1973):

$$K_d^{CA}(V_m) = K_d^{CA}(0) \cdot e^{\frac{z\delta FV}{RT}} \quad (3)$$

in which $K_d^{CA}(V_m)$ is the voltage-dependent dissociation constant of citrate, $K_d^{CA}(0)$ is the dissociation constant of citrate at 0 mV, V_m is the transmembrane potential, z is the valence of the blocker, δ is the fraction of the electrical membrane field traversed by the blocker, and F, R, and T are the Faraday constant, gas constant, and absolute temperature, respectively. Experiments were performed at room temperature (22°C–25°C).

For all calculations, the actual $citrate^{3-}$ concentration was determined with the Henderson-Hasselbach equation. The $citrate^{3-}$ concentration was estimated to be 93% of the different citric acid forms at pH 7.5.

The rectification rate coefficient was obtained by calculating the ratio between the conductance at the end of the activating pulse (V_m = −120 mV) and the conductance at the very beginning of the deactivating pulse (V_m = +60 mV). The conductance at the end of the activating pulse was estimated by using the ratio between the average current amplitude of the last 5 ms of the activation pulse and the applied activating potential. To calculate the conductance at the beginning of the deactivating pulse, the initial current was extrapolated from a monoexponential fit of the tail currents and divided by the applied deactivating potential of +60 mV.

Microsomal Protein Extraction and Protein Gel-Blot Analysis

Leaf material from unfiltrated (or empty vector-expressing) tobacco plants (data not shown) and AtALMT9-GFP-expressing tobacco plants was homogenized by cryogenic grinding with mortar and pestle and mixed with 4°C ice-cold homogenization buffer (250 mM Tris-HCl, pH 8.5, 25 mM EDTA, 30% Suc, 5 mM dithiothreitol, and protease inhibitor cocktail tablet [Roche]). The debris was sedimented by centrifugation at 5,000 rpm in a table-top centrifuge (Biofuge fresco; Heraeus) for 10 min at 4°C. Afterward, the supernatant fraction was passed through Miracloth (Calbiochem), transferred into ultracentrifugation tubes, and spun down at 35,000 rpm in an ultracentrifuge for 45 min at 4°C (Beckman Optima, SW41Ti). The membranes were solubilized in 100 μL of solubilization buffer (15 mM MOPS, pH 7.0, 1 mM EDTA, 30% glycerol [v/v], 0.5% *n*-dodecyl-β-D-maltoside, and protease inhibitor cocktail tablet [Roche]) for 30 min on ice. Equal protein amounts (Quick Start Bradford

Protein Assay; Bio-Rad) were loaded on SDS-PAGE gels (4%–20% Mini PROTEAN TGX precast gradient gel; Bio-Rad) in the absence of dithiothreitol. Proteins were blotted on polyvinylidene difluoride membranes (0.45 μm; Millipore) using the tank approach (Mini Trans-Blot Electrophoretic Transfer Cell; Bio-Rad), and an anti-GFP antibody (Clontech; 1:1,000) was used for immunodetection.

Sequence data from this article can be found in the GenBank/EMBL data libraries under accession numbers NP_188473.1.

Supplemental Data

The following materials are available in the online version of this article.

Supplemental Figure S1. AtALMT9$_{WT}$ and AtALMT9$_{K193E}$ are poorly permeable for citrate.

Supplemental Figure S2. Multiple alignment of the ALMT protein family of Arabidopsis.

Supplemental Figure S3. Intracellular localization of the different mutant channels of AtALMT9-GFP.

Supplemental Figure S4. AtALMT9 point mutants display different channel conductivity and sensitivity to citrate inhibition.

Supplemental Figure S5. The double mutant AtALMT9$_{K93E/E130K}$ is inhibited by intracellular citrate like AtALMT9$_{WT}$.

Received April 16, 2013; accepted August 5, 2013; published August 5, 2013.

LITERATURE CITED

Barbier-Brygoo H, De Angeli A, Filleur S, Frachisse JM, Gambale F, Thomine S, Wege S (2011) Anion channels/transporters in plants: from molecular bases to regulatory networks. Annu Rev Plant Biol **62:** 25–51

Becker D, Dreyer I, Hoth S, Reid JD, Busch H, Lehnen M, Palme K, Hedrich R (1996) Changes in voltage activation, Cs^+ sensitivity, and ion permeability in H5 mutants of the plant K^+ channel KAT1. Proc Natl Acad Sci USA **93:** 8123–8128

Bertl A, Blumwald E, Coronado R, Eisenberg R, Findlay G, Gradmann D, Hille B, Köhler K, Kolb HA, MacRobbie E, et al (1992) Electrical measurements on endomembranes. Science **258:** 873–874

Brandt B, Brodsky DE, Xue S, Negi J, Iba K, Kangasjärvi J, Ghassemian M, Stephan AB, Hu H, Schroeder JI (2012) Reconstitution of abscisic acid activation of SLAC1 anion channel by CPK6 and OST1 kinases and branched ABI1 PP2C phosphatase action. Proc Natl Acad Sci USA **109:** 10593–10598

Catterall WA (2010) Ion channel voltage sensors: structure, function, and pathophysiology. Neuron **67:** 915–928

Chen YH, Hu L, Punta M, Bruni R, Hillerich B, Kloss B, Rost B, Love J, Siegelbaum SA, Hendrickson WA (2010) Homologue structure of the SLAC1 anion channel for closing stomata in leaves. Nature **467:** 1074–1080

Choe S (2002) Potassium channel structures. Nat Rev Neurosci **3:** 115–121

Clay JR (1995) Quaternary ammonium ion blockade of IK in nerve axons revisited: open channel block vs. state independent block. J Membr Biol **147:** 23–34

Cotten JF, Welsh MJ (1999) Cystic fibrosis-associated mutations at arginine 347 alter the pore architecture of CFTR: evidence for disruption of a salt bridge. J Biol Chem **274:** 5429–5435

Cui G, Freeman CS, Knotts T, Prince CZ, Kuang C, McCarty NA (2013) Two salt bridges differentially contribute to the maintenance of cystic fibrosis transmembrane conductance regulator (CFTR) channel function. J Biol Chem**288:** 20758–20767

Daram P, Urbach S, Gaymard F, Sentenac H, Chérel I (1997) Tetramerization of the AKT1 plant potassium channel involves its C-terminal cytoplasmic domain. EMBO J **16:** 3455–3463

De Angeli A, Monachello D, Ephritikhine G, Frachisse JM, Thomine S, Gambale F, Barbier-Brygoo H (2006) The nitrate/proton antiporter AtCLCa mediates nitrate accumulation in plant vacuoles. Nature **442:** 939–942

De Angeli A, Zhang J, Meyer S, Martinoia E (2013) AtALMT9 is a malate-activated vacuolar chloride channel required for stomatal opening in Arabidopsis. Nat Commun **4:** 1804

Doyle DA, Morais Cabral J, Pfuetzner RA, Kuo A, Gulbis JM, Cohen SL, Chait BT, MacKinnon R (1998) The structure of the potassium channel: molecular basis of K^+ conduction and selectivity. Science **280:** 69–77

Dreyer I, Gomez-Porras JL, Riaño-Pachón DM, Hedrich R, Geiger D (2012) Molecular evolution of slow and quick anion channels (SLACs and QUACs/ALMTs). Front Plant Sci **3:** 263

Dutzler R, Campbell EB, Cadene M, Chait BT, MacKinnon R (2002) X-ray structure of a ClC chloride channel at 3.0 A reveals the molecular basis of anion selectivity. Nature **415:** 287–294

Ferrer-Montiel AV, Montal M (1996) Pentameric subunit stoichiometry of a neuronal glutamate receptor. Proc Natl Acad Sci USA **93:** 2741–2744

Furuichi T, Sasaki T, Tsuchiya Y, Ryan PR, Delhaize E, Yamamoto Y (2010) An extracellular hydrophilic carboxy-terminal domain regulates the activity of TaALMT1, the aluminum-activated malate transport protein of wheat. Plant J **64:** 47–55

Geelen D, Lurin C, Bouchez D, Frachisse JM, Lelièvre F, Courtial B, Barbier-Brygoo H, Maurel C (2000) Disruption of putative anion channel gene AtCLC-a in Arabidopsis suggests a role in the regulation of nitrate content. Plant J **21:** 259–267

Geiger D, Scherzer S, Mumm P, Marten I, Ache P, Matschi S, Liese A, Wellmann C, Al-Rasheid KAS, Grill E, et al (2010) Guard cell anion channel SLAC1 is regulated by CDPK protein kinases with distinct Ca^{2+} affinities. Proc Natl Acad Sci USA **107:** 8023–8028

Geiger D, Scherzer S, Mumm P, Stange A, Marten I, Bauer H, Ache P, Matschi S, Liese A, Al-Rasheid KA, et al (2009) Activity of guard cell anion channel SLAC1 is controlled by drought-stress signaling kinase-phosphatase pair. Proc Natl Acad Sci USA **106:** 21425–21430

Hechenberger M, Schwappach B, Fischer WN, Frommer WB, Jentsch TJ, Steinmeyer K (1996) A family of putative chloride channels from Arabidopsis and functional complementation of a yeast strain with a CLC gene disruption. J Biol Chem **271:** 33632–33638

Hedrich R (2012) Ion channels in plants. Physiol Rev **92:** 1777–1811

Hibbs RE, Gouaux E (2011) Principles of activation and permeation in an anion-selective Cys-loop receptor. Nature **474:** 54–60

Hilf RJ, Dutzler R (2009) Structure of a potentially open state of a proton-activated pentameric ligand-gated ion channel. Nature **457:** 115–118

Hoekenga OA, Maron LG, Piñeros MA, Cançado GMA, Shaff J, Kobayashi Y, Ryan PR, Dong B, Delhaize E, Sasaki T, et al (2006) AtALMT1, which encodes a malate transporter, is identified as one of several genes critical for aluminum tolerance in Arabidopsis. Proc Natl Acad Sci USA **103:** 9738–9743

Jentsch TJ (2008) CLC chloride channels and transporters: from genes to protein structure, pathology and physiology. Crit Rev Biochem Mol Biol **43:** 3–36

Kim TH, Böhmer M, Hu H, Nishimura N, Schroeder JI (2010) Guard cell signal transduction network: advances in understanding abscisic acid, CO_2, and Ca^{2+} signaling. Annu Rev Plant Biol **61:** 561–591

Kosari F, Sheng S, Kleyman TR (2006) Biophysical approach to determine the subunit stoichiometry of the epithelial sodium channel using the Xenopus laevis oocyte expression system. Methods Mol Biol **337:** 53–63

Kosari F, Sheng S, Li J, Mak DO, Foskett JK, Kleyman TR (1998) Subunit stoichiometry of the epithelial sodium channel. J Biol Chem **273:** 13469–13474

Kovermann P, Meyer S, Hörtensteiner S, Picco C, Scholz-Starke J, Ravera S, Lee Y, Martinoia E (2007) The Arabidopsis vacuolar malate channel is a member of the ALMT family. Plant J **52:** 1169–1180

Ligaba A, Katsuhara M, Ryan PR, Shibasaka M, Matsumoto H (2006) The *BnALMT1* and *BnALMT2* genes from rape encode aluminum-activated malate transporters that enhance the aluminum resistance of plant cells. Plant Physiol **142:** 1294–1303

Ligaba A, Kochian L, Piñeros M (2009) Phosphorylation at S384 regulates the activity of the TaALMT1 malate transporter that underlies aluminum resistance in wheat. Plant J **60:** 411–423

Linsdell P (2005) Location of a common inhibitor binding site in the cytoplasmic vestibule of the cystic fibrosis transmembrane conductance regulator chloride channel pore. J Biol Chem **280:** 8945–8950

MacKinnon R (1991) Determination of the subunit stoichiometry of a voltage-activated potassium channel. Nature **350:** 232–235

MacKinnon R, Yellen G (1990) Mutations affecting TEA blockade and ion permeation in voltage-activated K^+ channels. Science **250:** 276–279

Martinoia E, Meyer S, De Angeli A, Nagy R (2012) Vacuolar transporters in their physiological context. Annu Rev Plant Biol **63:** 183–213

Meyer S, Mumm P, Imes D, Endler A, Weder B, Al-Rasheid KAS, Geiger D, Marten I, Martinoia E, Hedrich R (2010) AtALMT12 represents an R-type anion channel required for stomatal movement in Arabidopsis guard cells. Plant J **63:** 1054–1062

Meyer S, Scholz-Starke J, De Angeli A, Kovermann P, Burla B, Gambale F, Martinoia E (2011) Malate transport by the vacuolar AtALMT6 channel in guard cells is subject to multiple regulation. Plant J **67:** 247–257

Motoda H, Sasaki T, Kano Y, Ryan PR, Delhaize E, Matsumoto H, Yamamoto Y (2007) The membrane topology of ALMT1, an aluminum-activated malate transport protein in wheat (Triticum aestivum). Plant Signal Behav **2:** 467–472

Mumm P, Imes D, Martinoia E, Al-Rasheid KA, Geiger D, Marten I, Hedrich R (January 12, 2013) C-terminus mediated voltage gating of Arabidopsis guard cell anion channel QUAC1. Mol Plant http://dx.doi.org/10.1093/mp/sst008

Negi J, Matsuda O, Nagasawa T, Oba Y, Takahashi H, Kawai-Yamada M, Uchimiya H, Hashimoto M, Iba K (2008) CO_2 regulator SLAC1 and its homologues are essential for anion homeostasis in plant cells. Nature **452:** 483–486

Neher E (1992) Correction for liquid junction potentials in patch clamp experiments. Methods Enzymol **207:** 123–131

Perutz MF (1978) Electrostatic effects in proteins. Science **201:** 1187–1191

Piñeros MA, Cançado GMA, Kochian LV (2008) Novel properties of the wheat aluminum tolerance organic acid transporter (TaALMT1) revealed by electrophysiological characterization in *Xenopus* oocytes: functional and structural implications. Plant Physiol **147:** 2131–2146

Rentsch D, Martinoia E (1991) Citrate transport into barley mesophyll vacuoles: comparison with malate-uptake activity. Planta **184:** 532–537

Robert A, Irizarry SN, Hughes TE, Howe JR (2001) Subunit interactions and AMPA receptor desensitization. J Neurosci **21:** 5574–5586

Roelfsema MRG, Hedrich R (2005) In the light of stomatal opening: new insights into 'the Watergate'. New Phytol **167:** 665–691

Rosenmund C, Stern-Bach Y, Stevens CF (1998) The tetrameric structure of a glutamate receptor channel. Science **280:** 1596–1599

Sasaki T, Yamamoto Y, Ezaki B, Katsuhara M, Ahn SJ, Ryan PR, Delhaize E, Matsumoto H (2004) A wheat gene encoding an aluminum-activated malate transporter. Plant J **37:** 645–653

Snyder PM, Cheng C, Prince LS, Rogers JC, Welsh MJ (1998) Electrophysiological and biochemical evidence that DEG/ENaC cation channels are composed of nine subunits. J Biol Chem **273:** 681–684

Traynelis SF, Wollmuth LP, McBain CJ, Menniti FS, Vance KM, Ogden KK, Hansen KB, Yuan H, Myers SJ, Dingledine R (2010) Glutamate receptor ion channels: structure, regulation, and function. Pharmacol Rev **62:** 405–496

Vahisalu T, Kollist H, Wang YF, Nishimura N, Chan WY, Valerio G, Lamminmäki A, Brosché M, Moldau H, Desikan R, et al (2008) SLAC1 is required for plant guard cell S-type anion channel function in stomatal signalling. Nature **452:** 487–491

von Heijne G, Gavel Y (1988) Topogenic signals in integral membrane proteins. Eur J Biochem **174:** 671–678

Ward JM, Mäser P, Schroeder JI (2009) Plant ion channels: gene families, physiology, and functional genomics analyses. Annu Rev Physiol **71:** 59–82

Waterhouse AM, Procter JB, Martin DM, Clamp M, Barton GJ (2009) Jalview version 2: a multiple sequence alignment editor and analysis workbench. Bioinformatics **25:** 1189–1191

Wittig I, Schägger H (2008) Features and applications of blue-native and clear-native electrophoresis. Proteomics **8:** 3974–3990

Woodhull AM (1973) Ionic blockage of sodium channels in nerve. J Gen Physiol **61:** 687–708

Yamaguchi M, Sasaki T, Sivaguru M, Yamamoto Y, Osawa H, Ahn SJ, Matsumoto H (2005) Evidence for the plasma membrane localization of Al-activated malate transporter (ALMT1). Plant Cell Physiol **46:** 812–816

Yang KY, Liu YD, Zhang SQ (2001) Activation of a mitogen-activated protein kinase pathway is involved in disease resistance in tobacco. Proc Natl Acad Sci USA **98:** 741–746

Yellen G, Jurman ME, Abramson T, MacKinnon R (1991) Mutations affecting internal TEA blockade identify the probable pore-forming region of a K^+ channel. Science **251:** 939–942